



Critical metallic phase in the overdoped random t - J model

Maine Christos^a, Darshan G. Joshi^a, Subir Sachdev^{a,b,1} , and Maria Tikhonovskaya^a 

Contributed by Subir Sachdev; received April 20, 2022; accepted June 6, 2022; reviewed by Ehud Altman and Chao-Ming Jian

We investigate a model of electrons with random and all-to-all hopping and spin exchange interactions, with a constraint of no double occupancy. The model is studied in a Sachdev–Ye–Kitaev-like large- M limit with $SU(M)$ spin symmetry. The saddle-point equations of this model are similar to approximate dynamic mean-field equations of realistic, nonrandom, t - J models. We use numerical studies on both real and imaginary frequency axes, along with asymptotic analyses, to establish the existence of a critical non-Fermi-liquid metallic ground state at large doping, with the spin correlation exponent varying with doping. This critical solution possesses a time-reparameterization symmetry, akin to Sachdev–Ye–Kitaev (SYK) models, which contributes a linear-in-temperature resistivity over the full range of doping where the solution is present. It is therefore an attractive mean-field description of the overdoped region of cuprates, where experiments have observed a linear- T resistivity in a broad region. The critical metal also displays a strong particle–hole asymmetry, which is relevant to Seebeck coefficient measurements. We show that the critical metal has an instability to a low-doping spin-glass phase and compute a critical doping value. We also describe the properties of this metallic spin-glass phase.

non-Fermi liquid | strange metal | cuprates

Recent experimental works have highlighted certain fundamental properties of cuprate superconductors and their complex and rich phase diagrams. One of the key aspects is a transformation in the normal state near an optimal doping $p = p_c$ (1–4) indicated most recently by thermal-Hall transport measurements (1, 3) and by photoemission experiments (4). While much attention has focused on the anomalous properties of the underdoped regime ($p < p_c$), it is often assumed that the overdoped regime ($p > p_c$) is a conventional Fermi liquid, and thus the latter has not attracted as much attention. However, careful experimental studies have reported significant strange-metal anomalies in transport properties also on the overdoped side (5–7). These observations indicate the presence of a non-Fermi-liquid metal in an extended doping region above optimal doping. On the underdoped side, recent experiments have established that there is a spin-glass phase (8, 9) in the La-based compounds.

Concordant with these observations, we present here a theoretical model with an extended non-Fermi-liquid phase at large dopings and a spin-glass phase at low doping.

Models with random interactions on a fully connected lattice in the Sachdev–Ye–Kitaev class (10, 11) yield a systematic route to studying non-Fermi liquids: The exact solutions of such models serve as dynamic mean-field theories of more realistic microscopic models (12–14). In this paper we report numerical and analytic solutions of a t - J model (Eq. 1) with random and all-to-all hopping and exchange interactions across a wide range of doping. The model has a global $SU(M)$ spin rotation symmetry, and we study a particular Sachdev–Ye–Kitaev (SYK)-like large- M limit with fermionic spinons. A previous study (15) found possible critical solutions of non-Fermi liquid metals by an analytic study of the low-energy limit of the saddle-point equations of this large- M limit. From renormalization group arguments it appeared that these possible critical solutions described only a critical point or a small range of intermediate doping and that a Fermi-liquid solution would appear in the overdoped regime.

The present paper presents a full numerical solution of these large- M saddle-point equations for a wide range of doping. The solutions are obtained on both the real and imaginary frequency axes, with mutually consistent results. We also supplement the numerical results with asymptotic analytic analyses. Our main results are that the Fermi liquid is never the solution of the large- M saddle-point equations and that one of the low-energy critical solutions obtained earlier (15) extends to an all-energy solution of the large- M equations in the entire overdoped regime. We further show that there is a phase transition to a low-doping spin-glass phase and construct a phase diagram (Fig. 1).

Notable features of the critical non-Fermi-liquid phase in Fig. 1 are as follows:

- 1) Spin correlations decay with an exponent that varies continuously with doping (unlike a Fermi liquid);

Significance

The strange metal state of the cuprate superconductors is the parent state from which many novel quantum phases emerge. Experiments have shown that the strange metal extends over a wider range of electron densities than previously believed. We show that a dynamic mean-field theory with random exchange interactions, in which the electron fractionalizes into excitations carrying its spin and charge, displays an extended strange metal regime. Several physical properties of this strange metal are in accord with experimental observations, including a linear-in-temperature contribution to the resistivity. At lower carrier density, our theory displays an instability to a spin glass, which is also observed. Our mean-field theory shows a route toward theories of quantum materials based upon more realistic microscopic models.

Author affiliations: ^aDepartment of Physics, Harvard University, Cambridge, MA 02138; and ^bSchool of Natural Sciences, Institute for Advanced Study, Princeton, NJ 08540

Author contributions: M.C., D.G.J., S.S., and M.T. designed research; M.C., D.G.J., S.S., and M.T. performed research; M.C., D.G.J., and M.T. analyzed data; and M.C., D.G.J., S.S., and M.T. wrote the paper.

Reviewers: E.A., University of California Berkeley; and C.J., Cornell University.

The authors declare no competing interest.

Copyright © 2022 the Author(s). Published by PNAS. This article is distributed under [Creative Commons Attribution-NonCommercial-NoDerivatives License 4.0 \(CC BY-NC-ND\)](https://creativecommons.org/licenses/by-nc-nd/4.0/).

¹To whom correspondence may be addressed. Email: sachdev@g.harvard.edu.

This article contains supporting information online at <https://www.pnas.org/lookup/suppl/doi:10.1073/pnas.2206921119/-DCSupplemental>.

Published July 15, 2022.

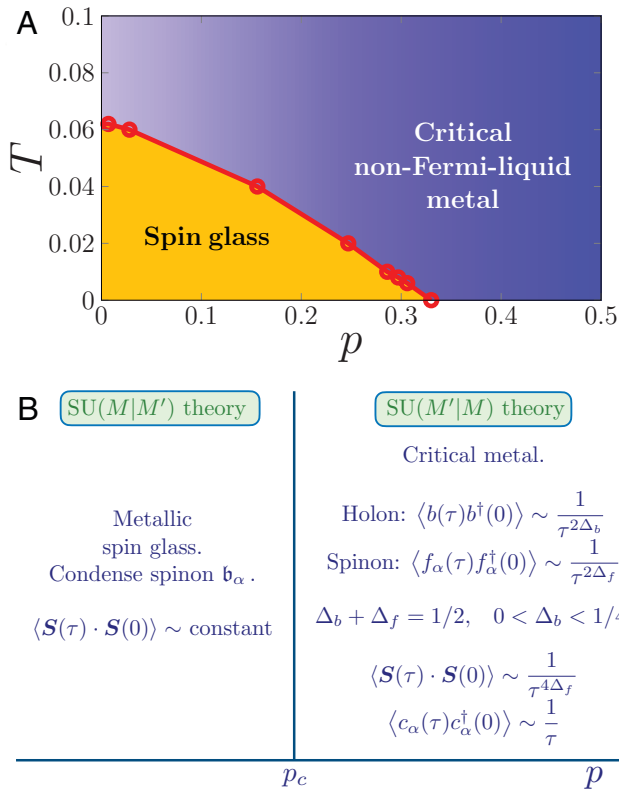


Fig. 1. (A) Phase diagram as a function of doping p and temperature T obtained from numerically solving the fermionic spinon large- M saddle-point equations of the random t - J model in Eq. 1 for $t = J = 1$. The red circles are critical doping value [$p_c(T)$] at a given temperature, obtained by looking at the spin-glass instability in the non-Fermi-liquid solution. The uncertainty for each p_c is within 0.003. The critical doping at $T = 0$ is obtained by directly solving the saddle-point equations on the real-frequency axis. (B) Properties of the $T = 0$ states. The low-doping spin-glass phase and large-doping critical-metal phase are separated by a quantum critical point at p_c . The critical metal has doping-dependent exponents $\Delta_{f,b}$ and a linear- T resistivity.

- 2) The electron correlators have the $\sim 1/\tau$ decay with imaginary time (as in a Fermi liquid), but with a pronounced particle-hole asymmetry (which is weak in a Fermi liquid); and
- 3) The mechanism of ref. 16 applies across the entire overdoped critical phase, and the resistivity has a linear- T contribution as $T \rightarrow 0$ at all dopings in this phase (unlike the T^2 resistivity in a Fermi liquid).

We also note here that there is a distinct large- M limit of the random t - J model (17) that yields a Fermi-liquid ground state at all nonzero doping. We discuss the relation to this limit in Section 4.

The plan of this paper is as follows: In Section 1 we introduce the model and discuss its general properties. In Section 2 we consider the critical solutions of the model introduced in Eq. 1 and show that there is a critical solution with doping-dependent exponents in the overdoped region. We then solve this model at zero temperature (Section 2.A), as well as finite temperature (Section 2.B), and show that it has an instability to a spin-glass phase. The results for spectral functions in the spin-glass phase are presented in Section 3 using an alternative bosonic spinon large- M limit. In both phases we report physical observables such as electron and spin spectral densities at both zero and finite temperatures. We conclude with a discussion and implication of our results in Section 4. Technical details and additional results are presented in SI Appendix.

1. Model

We consider a model of electrons with random and all-to-all hopping and exchange interaction with double occupancy being prohibited. This is the random t - J model that considers doping a random Heisenberg magnet (10). It is in the class of SYK models (10, 11) and is suitable for studying metallic phases obtained upon doping a Mott insulator. The Hamiltonian is

$$H = \frac{1}{\sqrt{N}} \sum_{i \neq j=1}^N t_{ij} c_{i\alpha}^\dagger c_{j\alpha} + \frac{1}{\sqrt{N}} \sum_{i < j=1}^N J_{ij} \vec{S}_i \cdot \vec{S}_j - \mu \sum_i c_{i\alpha}^\dagger c_{i\alpha}, \quad [1]$$

with the constraint, $\sum_\alpha c_{i\alpha}^\dagger c_{i\alpha} \leq 1$, since double occupancy is not allowed. In the above Hamiltonian, c_α is the electron annihilation operator with $\alpha = \uparrow, \downarrow$, the spin operator is $S_i^a = c_{i\alpha}^\dagger \sigma_{\alpha\beta}^a c_{i\beta} / 2$, and μ is the chemical potential. The complex hoppings t_{ij} and real exchange interactions J_{ij} are independent random numbers with zero mean and mean-square values t^2 and J^2 , respectively.

Note that one could also consider a t - J model with non-random nearest-neighbor hopping and nearest-neighbor random exchange interactions on a large-dimensional lattice. The on-site dynamical mean-field equations for such a model are the same as those obtained for the model in Eq. 1. It also allows for a definition of transport quantities such as resistivity.

We consider the problem at finite-hole doping (p). This was recently studied both analytically (15, 18) and numerically (19, 20). In particular, a deconfined critical-point scenario was proposed in ref. 15 to describe a quantum phase transition between a spin-glass phase at low doping with carrier density p and a Fermi-liquid phase at large doping with carrier density $1 + p$. The deconfined critical point proposed therein had the property that the local spin susceptibility was marginal as in the SYK models (10, 11). This was based on renormalization group arguments. However, a large- M analysis (15) led to two types of critical metallic solutions. One of the critical solutions corresponds to the deconfined critical point (although it is a phase in large- M limit), while the other was believed to be suppressed in favor of a Fermi-liquid phase.

In this work we find that, in fact, the second critical solution is stable, and a Fermi-liquid phase is never achieved within a large- M approach at the saddle-point level. This critical phase has the property that while the exponent of the spin correlation continuously varies with doping, the linear- T resistivity is present over the entire overdoped phase. This makes it an attractive candidate for the overdoped phase of cuprate in the light of recent experiments (5, 7). In the underdoped region, below a critical doping p_c , we find a spin-glass phase. Thus, the critical metal at large doping and spin-glass phase at small doping are separated by a quantum critical point at a finite doping p_c , as shown in Fig. 1.

As a result of the double-occupancy constraint each site has three states, namely empty ($|0\rangle$) and singly occupied ($|\uparrow\rangle$ and $|\downarrow\rangle$) states. These can be conveniently described using holon and spinon operators. The electron is thus fractionalized into holon and spinons. The critical metallic solutions in the overdoped region have gapless and critical fermionic spinons and bosonic holons (Section 2), while the underdoped spin-glass phase will be described by a fermionic holon and bosonic spinons (Section 3).

2. Critical Non-Fermi-Liquid Metal Phase

In this section, we show that our model in Eq. 1 admits a critical metallic solution. This phase is described by fermionic spinon (f_α) and bosonic holon (b) operators. The electron and

spin operators can be then written in terms of these fractional particles as

$$c_{i\alpha} = b^\dagger f_{i\alpha}, \quad S_i^a = f_{i\alpha}^\dagger \frac{\sigma_{\alpha\beta}^a}{2} f_{i\beta}, \quad [2]$$

with the constraint, $f_{i\alpha}^\dagger f_{i\alpha} + b_i^\dagger b_i = 1$. This theory realizes a $SU(1|2)$ superalgebra. The strategy to solve the model in Eq. 1 is to generalize to a larger symmetry. The spin index on the spinon operator (f_α) is generalized to $\alpha = 1, \dots, M$ and there is an additional orbital index for holon (b_ℓ) such that $\ell = 1, \dots, M'$. This theory realizes a $SU(M'|M)$ superalgebra. In this larger symmetry the electron and spin operators take the form

$$c_{\ell\alpha} = b_\ell^\dagger f_{i\alpha}, \quad S^a = f_{i\alpha}^\dagger T_{\alpha\beta}^a f_{i\beta}, \quad [3]$$

where the matrices T^a obey $SU(M)$ algebra. The constraint now takes the general form,

$$f_{i\alpha}^\dagger f_{i\alpha} + b_\ell^\dagger b_\ell = \kappa M. \quad [4]$$

The idea is to take a large- M' , M limit such that $k = M'/M$ is finite. This large- M limit is taken after we have performed a disorder average and taken the large-volume limit. Note that this large- M limit is distinct from the large- M limit in ref. 17, which had $M' = 1$; the latter limit leads to a Fermi-liquid phase at $T = 0$ at all nonzero doping.

A detailed analysis of our large- M limit can be found in refs. 15 and 18 and here we simply recall the saddle-point equations derived therein, which are

$$G_b(i\omega_n) = \frac{1}{i\omega_n + \mu_b - \Sigma_b(i\omega_n)}, \quad [5]$$

$$\Sigma_b(\tau) = -t^2 G_f(\tau) G_f(-\tau) G_b(\tau), \quad [6]$$

$$G_f(i\omega_n) = \frac{1}{i\omega_n + \mu_f - \Sigma_f(i\omega_n)}, \quad [7]$$

$$\Sigma_f(\tau) = -J^2 G_f(\tau)^2 G_f(-\tau) + kt^2 G_f(\tau) G_b(\tau) G_b(-\tau), \quad [8]$$

where G_b and G_f are the boson and fermion Green's functions, respectively, while Σ_b and Σ_f are the boson and fermion self-energies, respectively. Here τ is the imaginary time and ω_n are the Matsubara frequencies. The chemical potentials μ_f and μ_b are chosen to satisfy

$$\langle f^\dagger f \rangle = \kappa - kp, \quad \langle b^\dagger b \rangle = p. \quad [9]$$

We restrict our attention to the physical case, $\kappa = 1/2$ and $k = 1/2$. In terms of the holon and spinon Green's functions, the electron Green's functions and the spin correlator are

$$G_c(\tau) = -\langle T_\tau c_\alpha(\tau) c^\dagger(0) \rangle = -G_f(\tau) G_b(-\tau), \quad [10]$$

$$\chi(\tau) = \langle \vec{S}(\tau) \cdot \vec{S}(0) \rangle = -G_f(\tau) G_f(-\tau). \quad [11]$$

Similar equations have been obtained by a dynamic mean-field theory of a nonrandom t - J model on the square lattice, using a "noncrossing" approximation, and studied numerically (12, 13).

To solve the saddle-point equations on the imaginary-frequency axis, it is convenient to define

$$\beta\bar{\tau} = -G_b(i\omega_n = 0). \quad [12]$$

Then we can eliminate μ_b and obtain the following set of equations to solve:

$$G_b(i\omega_n) = \frac{1}{i\omega_n - 1/(\beta\bar{\tau}) - \Sigma_b(i\omega_n) + \Sigma_b(i\omega_n = 0)}, \quad [13]$$

$$\Sigma_b(\tau) = -t^2 G_f(\tau) G_f(-\tau) G_b(\tau), \quad [14]$$

$$G_f(i\omega_n) = \frac{1}{i\omega_n + \mu_f - \Sigma_f(i\omega_n)}, \quad [15]$$

$$\Sigma_f(\tau) = -J^2 G_f(\tau)^2 G_f(-\tau) + kt^2 G_f(\tau) G_b(\tau) G_b(-\tau), \quad [16]$$

$$-G_b(\tau = 0^-) = p, \quad [17]$$

$$G_f(\tau = 0^-) = \kappa - kp. \quad [18]$$

Thus, we have six equations to solve for the six variables $\bar{\tau}$, μ_f , G_f , G_b , Σ_f , and Σ_b . Note that Eq. 13 holds for all ω_n .

A. Real-Frequency Solution at Zero Temperature. In this section we discuss the solutions of the saddle-point equations on the real-frequency axis at $T = 0$. The details of real-frequency equations corresponding to Eqs. 13–18 can be found in [SI Appendix, section 1](#). We look for a low-frequency conformal solution for the fermion and boson Green's functions with the following form:

$$G_a(i\omega_n) = -iC_a \begin{pmatrix} e^{-i\theta_a} \\ -e^{i\theta_a} \end{pmatrix} \frac{1}{|\omega|^{1-2\Delta_a}}, \quad [19]$$

where the subscript $a = f, b$ corresponds to the fermion and boson Green's functions, respectively. In the above ansatz, C_a is a constant, θ_a is an asymmetry parameter, and Δ_a is the exponent determining the critical solution. Below we discuss the relation between these parameters and different possible solutions. The vector notation is introduced to denote the positive and negative frequency parts of the solution. Using this form of Green's function, it is then straightforward to write the corresponding spectral densities,

$$\begin{aligned} \rho_a(\omega) &= -\frac{1}{\pi} \text{Im}[G_a(i\omega_n = \omega + i0^+)] \\ &= \frac{C_a}{\pi} \begin{pmatrix} \sin(\pi\Delta_a + \theta_a) \\ \sin(\pi\Delta_a - \theta_a) \end{pmatrix} \frac{1}{|\omega|^{1-2\Delta_a}}. \end{aligned} \quad [20]$$

The exponents of the fermion and boson Green's functions satisfy the constraint $\Delta_f + \Delta_b = 1/2$. The ansatz considered in Eq. 19 admits three types of solutions (15):

- 1) $\Delta_f = \Delta_b = 1/4$: This is the solution that leads to a marginal spin correlation, i.e., a $1/\tau$ decay as in the SY spin liquid (10) found in the insulating case. In ref. 18 it was shown that such a solution exists only in a very small doping range near $p = 0$. This is also the solution that corresponds to the deconfined critical point discussed in ref. 15. We do not discuss this solution any further here, because we believe the actual ground state at very low doping is a spin glass.
- 2) $\Delta_b = 0, \Delta_f = 1/2$: Such a solution would be the analog of the Fermi-liquid solution found in the large- M limit of ref. 17. However, it turns out that such a solution is not a valid solution of the saddle-point equations of the large- M limit considered here. We provide more details in [SI Appendix, section 1.B](#) in this regard.
- 3) $1/4 < \Delta_f < 1/2$: In this solution the J term in the fermion self-energy in Eq. 16 is subdominant at low energies, although it does have contributions at higher energies. This solution

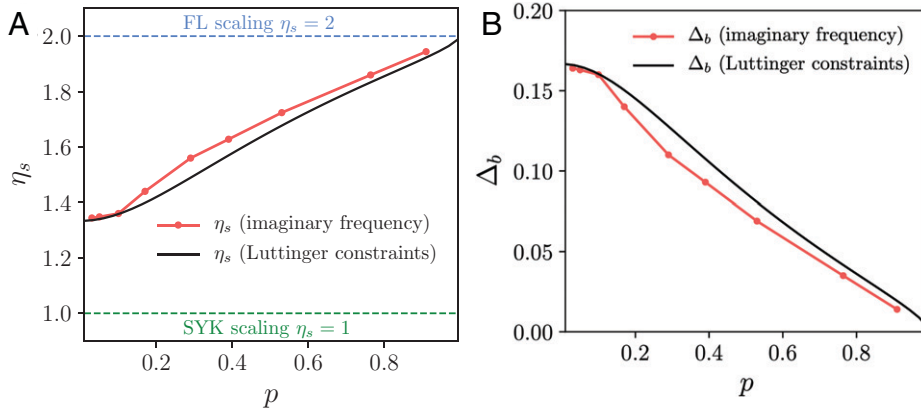


Fig. 2. (A) We plot the doping dependence of the exponent η_s of the spin correlation $\chi(\tau) \sim 1/|\tau|^{\eta_s}$. We compute $\eta_s = 2 - 4\Delta_b$ in two independent ways, one by solving the Luttinger relations and the zero-frequency saddle-point equations at $T = 0$ as explained in the text (black curve) and one by computing η_s from the value of Δ_b obtained from the imaginary-frequency numerics (red curve), as discussed in Section 2. We find the two results in good agreement. At $p = 0$ we obtain $\eta_s = 4/3$, with η_s increasing monotonically with increasing doping such that $\eta_s \rightarrow 2$ as $p \rightarrow 1$. (B) We plot the doping dependence of Δ_b as obtained independently from the Luttinger relations and $T = 0$ zero-frequency saddle-point equations and from solving the imaginary-frequency saddle-point equations. We find at $p = 0$ $\Delta_b = 1/6$ and $\Delta_b \rightarrow 0$ as $p \rightarrow 1$. Consequently, this means $\Delta_f = 1/3$ at $p = 0$ and $\Delta_f \rightarrow 1/2$ as $p \rightarrow 1$.

results in doping-dependent exponents. As we shall see below, we find this solution to be present for all values of doping, and it will be a valid solution in the overdoped region. Our subsequent analyses in this section focus on this solution.

We now briefly discuss our strategy to find solution 3 and more details can be found in *SI Appendix, section 1*. The conformal solution ansatz introduced in Eq. 19 satisfies two Luttinger constraints (15, 18),

$$\begin{aligned} \frac{\theta_f}{\pi} + \left(\frac{1}{2} - \Delta_f\right) \frac{\sin(2\theta_f)}{\sin(2\pi\Delta_f)} &= \frac{1}{2} - \kappa + kp, \\ \frac{\theta_b}{\pi} + \left(\frac{1}{2} - \Delta_b\right) \frac{\sin(2\theta_b)}{\sin(2\pi\Delta_b)} &= \frac{1}{2} + p. \end{aligned} \quad [21]$$

For solution 3 the constants C_f and C_b cannot be determined individually but their product is a constant. This leads to another constraint involving θ_s and Δ_s as shown in ref. 15:

$$k = -\frac{\Gamma(2 - 2\Delta_f)\Gamma(2\Delta_f) \sin(\pi\Delta_f + \theta_f) \sin(\pi\Delta_f - \theta_f)}{\Gamma(2 - 2\Delta_b)\Gamma(2\Delta_b) \sin(\pi\Delta_b + \theta_b) \sin(\pi\Delta_b - \theta_b)}, \quad [22]$$

where $k = 1/2$ in our case. Together with the constraint $\Delta_f + \Delta_b = 1/2$ and Eqs. 21 and 22, there are four equations to solve for four variables, namely Δ_f , Δ_b , θ_f , and θ_b , at a fixed doping p . Solving these equations gives us these parameters as a function of doping, as shown in Fig. 2 and *SI Appendix, Fig. S3*. Determination of the constants C_f and C_b requires full solution of the saddle-point equation at all frequencies, and the resulting values are shown in *SI Appendix, Fig. S3*. Of particular interest is the doping dependence of Δ_b , shown in Fig. 2.

In the large- M limit, from Eq. 11 it is clear that the anomalous dimension of the electron operator is $\eta_c = 2(\Delta_f + \Delta_b) = 1$ and that of the spin operator is $\eta_s = 4\Delta_f = 2 - 4\Delta_b$. Therefore, from Eq. 11, as a function of the imaginary time the electron Green's function and the local spin correlation have the form

$$G_c(\tau) \sim \frac{1}{\tau}, \quad \chi(\tau) \sim \frac{1}{\tau^{2-4\Delta_b}}. \quad [23]$$

Thus, we find that although the electron Green's function is Fermi liquid-like, the spin correlation is not. Therefore, the solution we

have found is a critical metallic phase with a doping-dependent exponent of the spin correlation. Only in the limit $p \rightarrow 1$ we have $\Delta_b \rightarrow 0$, leading to a Fermi-liquid-like spin correction with a $1/\tau^2$ decay.

Having established the presence of solution 3, we now solve the saddle-point equations on the real-frequency axis numerically to obtain the full ω dependence of the boson and fermion spectral densities. Using these we can also obtain the electron and spin spectral densities. *SI Appendix, Fig. S1* shows the full ω -dependent solution for the fermion and boson spectral densities, while in Fig. 3 we plot the electron and spin spectral densities. The boson and fermion spectral densities have the form $\rho_a(\omega) \sim \omega^{2\Delta_a-1}$ with $a = f, b$. Since $\Delta_a < 1/2$, we plot the rescaled spectral densities in *SI Appendix, Fig. S1*. Note that the fermion and boson spectral densities are not observable quantities. However, the electron and spin spectral densities are observable in photoemission and neutron scattering experiments. These are defined as follows:

$$\rho_c = -\frac{1}{\pi} \text{Im}[G_c(i\omega \rightarrow \omega + i0^+)] \quad [24]$$

$$\rho_s = \frac{1}{\pi} \text{Im}[\chi(i\omega \rightarrow \omega + i0^+)] = \frac{1}{\pi} \chi''(\omega). \quad [25]$$

In *SI Appendix, section 1* we present more details on evaluating these spectral densities.

As noted above, the most striking feature of our solution is a continuously varying spin-correlation exponent. This is clearly seen in Fig. 2A, which shows the exponent of the spin correlator $\chi(\tau) \sim 1/|\tau|^{\eta_s}$ where $\eta_s = 4\Delta_f$, and in Fig. 3B, where $\chi''(\omega) \sim \text{sgn}(\omega)|\omega|^{4\Delta_f-1}$ at low frequencies. Only in the limit $p \rightarrow 1$ do we see a Fermi-liquid-like behavior, $\chi''(\omega) \sim \omega$, as $\Delta_f \rightarrow 1/2$. The electron spectral density is a constant in the low-frequency limit with different values for $\omega \rightarrow 0^+$ and $\omega \rightarrow 0^-$ (Fig. 3A), thus resulting in a discontinuity at $\omega = 0$. It clearly displays a particle-hole asymmetry throughout this phase, which is relevant in the context of understanding the measurement of the Seebeck coefficient in recent experiments (21, 22).

As for the SYK model (14), the conformal solutions to Eqs. 5–8 have time reparameterization symmetry when the self-energies are singular so that $G_{f,b}(i\omega_n)\Sigma_{f,b}(i\omega_n) \approx -1$. Ref. 16 discussed a mechanism relating the time reparameterization symmetry to a linear- T contribution to the resistivity, and the same mechanism applies to the cases 2 and 3 above. Briefly, to obtain a model with

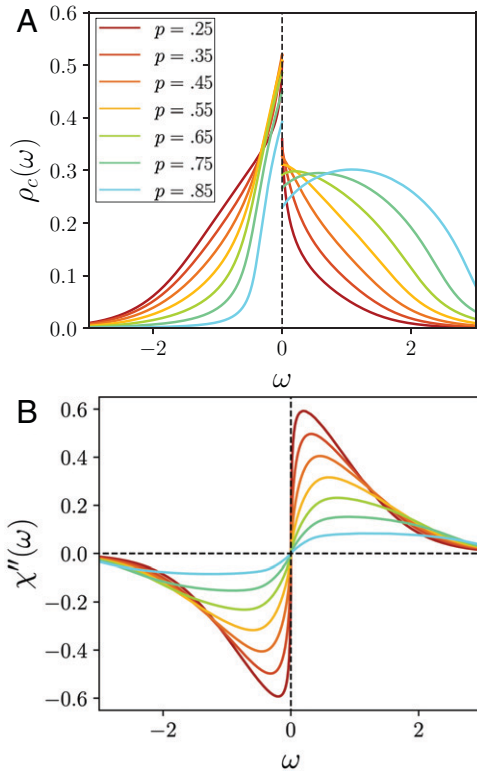


Fig. 3. Plot of the electron spectral density (A) and spin spectral density (B) obtained at $t = j = 1$. Shown is the electron spectral density that discontinuously approaches two different constants $\omega = 0$, leading to $1/\tau$ decay of the electron density in imaginary time. The spin spectral density goes as $\text{sgn}(\omega)|\omega|^{4\Delta_f - 1}$ as $\omega \rightarrow 0$. Only for large p do we have Δ_f approach $1/2$, which implies a linear frequency dependence and $1/\tau^2$ decay behavior in imaginary time characteristic of a Fermi liquid.

spatial structure, we consider the t - J model on a large-dimension lattice with nonrandom t_{ij} but random nearest-neighbor J_{ij} . In the limit of large dimension, the self-energies become local, and the Green's functions and self-energies obey equations closely related to Eqs. 5–8. The conductivity in this large-dimension model is given by the Kubo formula applied at one loop to the electron Green's function. The identity $\Delta_f + \Delta_b = 1/2$ implies that $G_c \sim 1/\tau$, and inserting this leading scaling behavior into the Kubo formula leads to a T -independent residual resistivity. To obtain temperature dependence, we consider the corrections to scaling from the time reparameterization operator, whose scaling dimension $h = 2$ leads to corrections that depend linearly on T or ω . Applying such a correction to the residual resistivity, we obtain a linear-in- T resistivity. The critical metal phase found here is therefore an attractive candidate for the overdoped cuprates. We also note that our solution is consistent with the findings of recent numerical work on a similar model (20), as we discuss further in Section 4.

B. Imaginary-Frequency Solution. We also numerically solve Eqs. 13–18 on the imaginary-frequency axis at finite temperatures and for different doping values. A critical metallic solution is found for all values of doping. We calculate the part on Green's functions as well as gauge-invariant observables, namely, electron Green's function and spin correlation. These are shown in Fig. 4. The exponent of the bosonic Green's function, Δ_b , introduced in Eq. 19 can be determined from the temperature dependence of $G_b(i\omega = 0)$. In the low-temperature limit, the bosonic Green's function of the critical metallic solution has a conformal form at low frequencies, which follows the relation

$$G_b(i\omega = 0) = C_0 T^{-1+2\Delta_b}, \quad [26]$$

where C_0 is some constant and T is the temperature. To extract Δ_b from the data, we plot $\log(G_b(i\omega = 0))$ as a function of $\log(T)$ and perform a linear fit. The slope of this linear fit then determines Δ_b . In Fig. 2 we plot Δ_b determined from this procedure as a function of doping. It is in good agreement with the result obtained from analytic solution (shown as black curve in Fig. 2) discussed in Section 2. The lowest temperature that we used for the procedure is $T = 0.01$.

In SI Appendix, section 2 we present additional results obtained from solving the saddle-point equations on the imaginary-frequency axis. In particular, we calculate the electron Green's function and the spin correlation, which are physical observables. We find that the spin correlation $\chi(\tau)$ fits the conformal form to a very high accuracy and this allows us to extract the corresponding exponent. Moreover, using Padé approximation, we also perform a numerical analytic continuation to the real-frequency axis to obtain the electron and spin spectral densities. These are discussed in SI Appendix, section 2.C, and are in remarkable agreement with those obtained from real-frequency analysis at zero temperature.

C. Instability to Spin-Glass Phase/Quantum Critical Point. The critical metallic solution discussed above is expected to be stable at large doping values. In the low-doping region we expect a spin-glass phase, which is connected to the spin-glass phase found in the insulating case (23). The critical metallic phase and the spin-glass phase are separated by a quantum critical point at a finite doping. The critical value of doping can be estimated using a Ginzburg-Landau-type free energy considered in ref. 23. It was derived by considering fluctuations over the saddle point leading to a $1/M$ correction and it has a form,

$$\mathcal{F} = \left[1 - \frac{J^2}{M} \chi^2(i\omega = 0) \right] \Psi^2 + \dots, \quad [27]$$

where $\chi(i\omega = 0) = \int_0^\beta \chi(\tau) d\tau$ is the local spin susceptibility and Ψ is the spin-glass order parameter. In the insulating $p = 0$ phase studied in ref. 23, it was found that $\chi(i\omega = 0)$ diverged logarithmically at $T = 0$ because the spin exponent has the “marginal” value $\eta_s = 1$. Consequently, the coefficient of Ψ^2

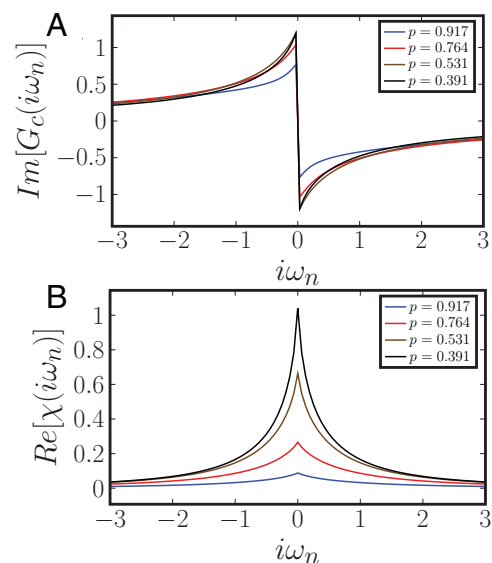


Fig. 4. (A) Imaginary part of the electron Green's function on the Matsubara-frequency axis at $T = 0.01$ for different dopings. (B) Real part of the spin correlation on the Matsubara-frequency axis at $T = 0.01$ for different dopings. We have used $t = j = 1$.

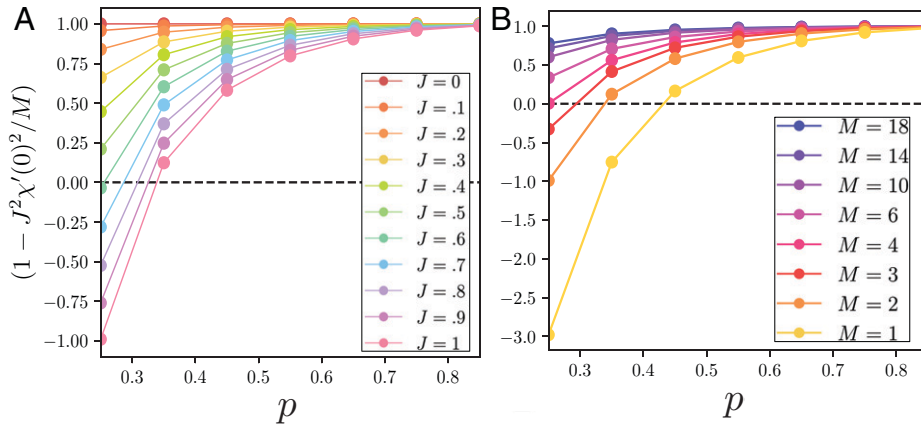


Fig. 5. Plots of the coefficient of the quadratic term in the free energy in Eq. 27 as a function of doping for (A) different values of J with $t = 1$ and $M = 2$ and (B) different values of M with $t = J = 1$. In both plots, $T = 0$.

is always negative as $T \rightarrow 0$, and spin-glass order is present at $T = 0$. In our non-Fermi-liquid solution, $\eta_s < 1$, and so $\chi(i\omega = 0)$ is finite at $T = 0$: This allows the possibility of $\Psi = 0$ and no spin-glass order at $T = 0$. We find in the overdoped region the coefficient of the quadratic term is positive and the free energy is thus minimized by $\Psi = 0$. On the other hand, in the underdoped region this coefficient is negative, leading to a nonzero spin-glass order parameter. A change in the sign of the coefficient of Ψ^2 at $T = 0$ thus indicates a quantum phase transition to a spin-glass phase and can be used to estimate the critical value of doping. We plot this coefficient at zero temperature in Fig. 5A as a function of doping for different values of J at $M = 2$. We clearly see that for larger values of J there is a quantum phase transition at a finite doping. In particular, for $J = 1$ we find $p_c \approx 0.33$ and for $J = 0.5$ we get $p_c \approx 0.25$. Similarly, in Fig. 5B we plot the coefficient in Eq. 27 as a function of doping for different values of M at a fixed $J = 1$ at zero temperature. It is clear that for large values of M there is no phase transition. We also plot the critical value of M as a function of doping in Fig. 6 at zero temperature. We perform a similar analysis at finite temperature to obtain the critical doping as a function of temperature (SI Appendix, Fig. S8). The resulting phase diagram is shown in Fig. 1A. The spin-glass susceptibility increases with decreasing temperature and thus the spin-glass phase is found upon cooling the non-Fermi liquid at low doping. However, note that unlike in the case of the random Heisenberg model (10, 24) (where solution 1 with $\Delta_f = \Delta_b = 1/4$ is present) the spin-glass susceptibility does not diverge at low temperature in the present case. This is one of the important reasons for a stable critical

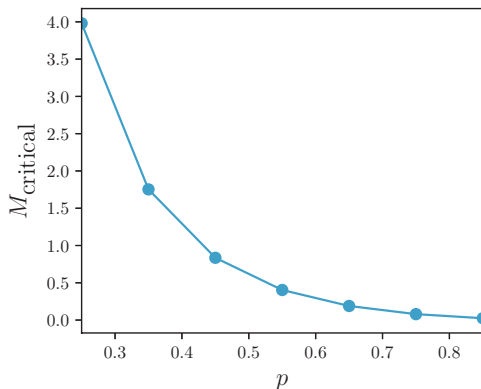


Fig. 6. Plot showing critical value of M for which the coefficient of the quadratic term in free energy Eq. 27 changes sign at zero temperature.

solution at zero temperature in a broad doping region. We also note that while $1/M$ corrections are used in deriving the form of Eq. 27, we have used the $M \rightarrow \infty$ solution for the critical metal to compute $\chi'(0)$ as it appears in Eq. 27. While a more accurate estimate of p_c may be obtained by adding $1/M$ corrections to the critical metal solution, we emphasize that the $M \rightarrow \infty$ solution is sufficient to capture existence of a finite-doping phase transition between the spin glass and critical metal.

3. Spin-Glass Phase

In this section we discuss the spin-glass phase present at lower dopings. In this case, we use the representation where spinons are bosonic (b) and the holon is a fermion operator (f). In terms of these operators,

$$c_\alpha = f^\dagger b_\alpha, \quad \vec{S} = b_\alpha^\dagger \frac{\vec{\sigma}_{\alpha\beta}}{2} b_\beta, \quad [28]$$

and we realize a $SU(2|1)$ superalgebra. Just as before, we now enlarge the symmetry here to $SU(M|M')$, which means $\alpha = 1, \dots, M$ and the holon operator acquires an index $\ell = 1, \dots, M'$. Note that this bosonic spinon large- M limit is distinct from the fermionic spinon large- M limit followed in Section 2, and the two models are the same only for $M = 2$; so there is no reason to expect quantitative agreement between the results of the present section and those of Section 2.

The strategy to obtain the saddle-point equations is similar to that discussed earlier in Section 2. From refs. 15 and 18 we have

$$\begin{aligned} G_b(i\omega_n) &= \frac{1}{i\omega_n + \mu_b - \Sigma_b(i\omega_n)}, \\ G_f(i\omega_n) &= \frac{1}{i\omega_n + \mu_f - \Sigma_f(i\omega_n)}, \\ \Sigma_b(\tau) &= -kt^2 G_f(\tau) G_f(-\tau) G_b(\tau) + J^2 G_b(\tau)^2 G_b(-\tau), \\ \Sigma_f(\tau) &= t^2 G_f(\tau) G_b(-\tau) G_b(\tau), \\ G_b(\tau = 0^-) &= -\kappa + kp, \\ G_f(\tau = 0^-) &= p. \end{aligned}$$

Physically, the spin-glass phase can be understood as a condensation of bosonic spinons. Contrary to the earlier case, since we are interested in the spin-glass phase, we need to retain the replica off-diagonal terms in the action upon disorder averaging. There is, however, some simplification and only replica off-diagonal components of the bosonic Green's function at $i\omega_n = 0$

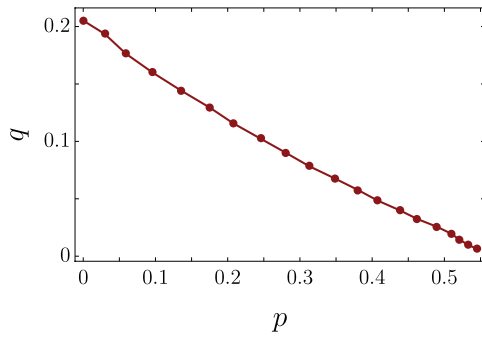


Fig. 7. Plot of spin-glass order parameter, $q = g^2$, as a function of doping obtained by solving the bosonic spinon saddle-point Eqs. 29–34 on the real-frequency axis at $T = 0$. The point at $p = 0$ is obtained by solving *SI Appendix*, Eqs. S65–S67 at zero temperature on the real-frequency axis. The parameters of the model are $J = t = 1$. The critical doping p_c at which the spin-glass order vanishes in the present bosonic spinon computation need not be the same as that in the fermionic spinon computation in *Section 2.C* because the models are identical only for $M = 2$.

are relevant. These are captured via the parameter g that is related to the spin-glass order parameter, as discussed in detail in *SI Appendix*, section 3. After incorporating the spin-glass order in $G_b(\tau) = G_r(\tau) - g$, we obtain the following saddle-point equations:

$$[G_r(i\omega_n)]^{-1} = i\omega_n - \frac{Jg}{\Theta} - [\Sigma_r(i\omega_n) - \Sigma_r(i\omega_n = 0)], \quad [29]$$

$$G_f(i\omega_n) = \frac{1}{i\omega_n + \mu_f - \Sigma_f(i\omega_n)}, \quad [30]$$

$$\begin{aligned} \Sigma_r(\tau) = J^2 & \left([G_r(\tau)]^2 G_r(-\tau) - 2gG_r(\tau)G_r(-\tau) \right. \\ & \left. - g[G_r(\tau)]^2 + 2g^2G_r(\tau) + g^2G_r(-\tau) \right) \\ & - kt^2 G_f(\tau)G_f(-\tau) (-g + G_r(\tau)), \end{aligned} \quad [31]$$

$$\begin{aligned} \Sigma_f(\tau) = t^2 G_f(\tau) & \left(g^2 - gG_r(\tau) - gG_r(-\tau) \right. \\ & \left. + G_r(-\tau)G_r(\tau) \right), \end{aligned} \quad [32]$$

$$g - G_r(\tau = 0^-) = \kappa - kp, \quad [33]$$

$$G_f(\tau = 0^-) = p. \quad [34]$$

The dimensionless parameter $\Theta = 1/\sqrt{3}$, as detailed in *SI Appendix*, section 3. We solve the above equations on real and imaginary-frequency axes. The main observable in this phase is the spin-glass order parameter, which we plot as a function of doping in Fig. 7 at zero temperature. The spin-glass order parameter is finite at lower dopings and decreases upon increasing doping. We show results for the order parameter computed for small but finite temperature obtained using the imaginary frequency analysis in *SI Appendix*, section 4. We also calculate the holon and spinon Green's functions as well as the electron Green's function and spin correlation at finite temperature. These quantities are detailed in the same *SI Appendix*, section 4.

We solve the saddle-point equations Eqs. 29–34 at zero temperature to obtain the fermion and boson spectral functions, as well as the electron and spin spectral functions for a range of doping. In terms of the spinon and holon spectral functions the electron spectral function has the following form:

$$\rho_c(\omega) = \int_0^\omega d\omega_1 \rho_r(\omega_1) \rho_f(\omega_1 - \omega) + g\rho_f(-\omega). \quad [35]$$

Similarly, we obtain the expression for the spin spectral function,

$$\begin{aligned} \rho_s(\omega) = g^2 \beta \omega \delta(\omega) + g [\rho_r(\omega) - \rho_r(-\omega)] \\ - \int_0^\omega d\omega_1 \rho_r(\omega_1) \rho_r(\omega - \omega_1), \end{aligned} \quad [36]$$

as in ref. 24. The spectral functions at zero temperature for different values of doping are shown in Fig. 8. We note that the boson spectral function behaves linearly with frequency at small frequencies. Consequently, the spin spectral function also depends linearly on ω at small frequencies. We also note the double-peak structure in the electron spectral function $\rho_c(\omega)$ in Fig. 8B. Recall that the electron spectral function is a convolution of the spinon and holon spectral functions, as well as a term proportional to $g\rho_f(-\omega)$. At small dopings the value of g is larger and hence there is a dominant peak coming from the fermion spectral function. As g decreases with increasing doping the contribution from the boson spectral function increases, leading to the second peak at positive frequencies. All the spectral functions satisfy the respective sum rules, which are detailed in *SI Appendix*, section 4.B.

Apart from the numerical analysis at zero temperature, we also perform a Pade-approximation-based numerical analytic continuation of the imaginary-axis solution obtained at finite temperature. We evaluate the holon, spinon, electron, and spin spectral densities at finite temperature. These are discussed in *SI Appendix*, section 2.C, and are consistent with those obtained from real-frequency calculation at zero temperature for some range of doping.

4. Discussion

We have presented a large- M solution for the random t - J model for the entire doping range. Our main finding is a critical non-Fermi-liquid metal phase at large dopings. This phase is characterized by a spin correlation exponent that varies

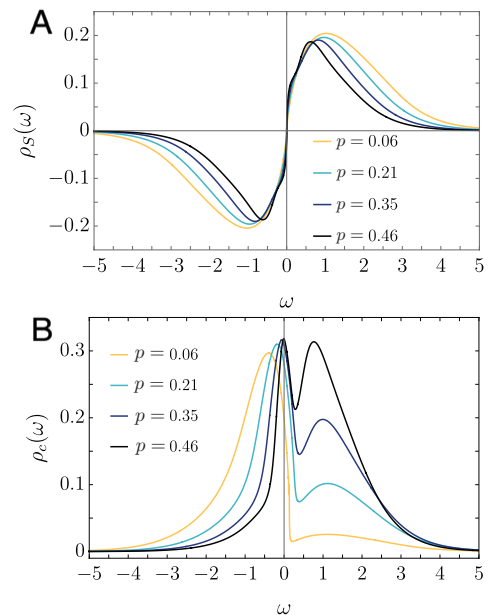


Fig. 8. Spin spectral function (A) and electron spectral function (B) obtained at zero temperature via real-frequency analysis for several values of doping. Note the linear in frequency behavior at small frequencies for $\rho_s(\omega)$. Parameters are $J = t = 1$.

continuously with doping, a linear in temperature contribution to the resistivity as $T \rightarrow 0$, and an electron spectral function with a Fermi-liquid-like decay at long time, but with a pronounced particle-hole asymmetry. This critical phase captures many aspects of experimental observations in the overdoped cuprates. It has been observed that in the overdoped region of cuprate materials there is a broad range of doping where the resistivity displays a linear- T behavior (5, 7). Our findings propose a possible mechanism for this observation. Also, recent Seebeck coefficient measurements (21, 22) hint toward a particle-hole asymmetric electron spectral density, which our solution also displays. It turns out that in our solution the electron Green's function appears Fermi liquid-like although the spin correlation does not. This may also explain the fact that experiments on overdoped cuprates probing electron Green's function directly, such as photoemission (4), may observe a Fermi-liquid behavior and cannot access the critical phase. However, transport measurements obtain properties such as linear- T resistivity, which is starkly in contrast to a Fermi liquid.

We also show that the overdoped critical phase has an instability toward a spin-glass phase at lower dopings. The spin-glass phase is characterized by a spin-glass order parameter, which we calculate using bosonic spinons. We show that this order parameter decreases upon increasing doping. In the context of cuprates, recent experiments have reported the presence of a spin-glass phase at low doping (9). Our work therefore presents a comprehensive analysis of the model in Eq. 1 at variable doping and captures the quantum phase transition between the spin-glass phase and a critical non-Fermi-liquid metal. We also note that our results are consistent with recent numerical work on a related model (20).

A notable feature of our results is that we never find a Fermi-liquid phase in our large- M limit of the t - J model, as discussed in *SI Appendix, section 1.B*. This is in contrast to the distinct large- M limit of ref. 17, in which the boson b condenses at all

nonzero p , leading to a Fermi-liquid phase at all doping. The two large- M limits coincide only for the physical value $M = 2$, and it is an open question which large- M limit yields the correct picture at $M = 2$ for the random t - J model. However, we note that the numerical study of the $M = 2$ case in ref. 20 does show indications of non-Fermi-liquid behavior in the overdoped regime over the T range studied, as their measured spin exponent η_s varies with doping in a manner consistent with Fig. 2A. Thus, although a Fermi-liquid phase may eventually appear at very low T in the overdoped regime for $M = 2$, it does appear that our non-Fermi-liquid solution is an attractive description of the physics over a wide range of temperatures and dopings accessible in numerics and experiments.

In conclusion, our work presents a critical metallic phase as an attractive candidate for the overdoped cuprates that matches observations over a significant temperature range. This phase is obtained for a model with random and all-to-all interactions. Although such a model is far from the microscopic Hamiltonian of the cuprates, the saddle-point equations solved are closely related to dynamic mean-field equations of more realistic models in finite dimensions (12, 13), as has been extensively discussed in a recent review (14). At very low temperatures, we ultimately expect a cross-over to behavior characteristic of finite-dimensional systems, and describing this cross-over remains an important topic for future research.

Data Availability. All study data are included in this article and/or *SI Appendix*. Code is available upon reasonable request.

ACKNOWLEDGMENTS. This research was supported by the US NSF Grant DMR-2002850 by the Simons Collaboration on Ultra-Quantum Matter, which is a grant from the Simons Foundation (651440, to S.S.). D.G.J. acknowledges support from the Leopoldina fellowship by the German National Academy of Sciences through Grant LPDS 2020-01.

1. C. Proust, L. Taillefer, The remarkable underlying ground states of cuprate superconductors. *Annu. Rev. Condens. Matter Phys.* **10**, 409–429 (2019).
2. B. Michon *et al.*, Thermodynamic signatures of quantum criticality in cuprate superconductors. *Nature* **567**, 218–222 (2019).
3. S. Badoux *et al.*, Change of carrier density at the pseudogap critical point of a cuprate superconductor. *Nature* **531**, 210–214 (2016).
4. S. D. Chen *et al.*, Incoherent strange metal sharply bounded by a critical doping in Bi2212. *Science* **366**, 1099–1102 (2019).
5. R. A. Cooper *et al.*, Anomalous criticality in the electrical resistivity of $\text{La}_{2-x}\text{Sr}_x\text{CuO}_4$. *Science* **323**, 603–607 (2009).
6. R. L. Greene, P. R. Mandal, N. R. Poniatowski, T. Sarkar, The strange metal state of the electron-doped cuprates. *Annu. Rev. Condens. Matter Phys.* **11**, 213–229 (2020).
7. J. Ayres *et al.*, Incoherent transport across the strange-metal regime of overdoped cuprates. *Nature* **595**, 661–666 (2021).
8. C. Panagopoulos *et al.*, Exposing the spin-glass ground state of the nonsuperconducting $\text{La}_{2-x}\text{Sr}_x\text{Cu}_{1-y}\text{Zn}_y\text{O}_4$ high- T_c oxide. *Phys. Rev. B Condens. Matter Mater. Phys.* **69**, 144510 (2004).
9. M. Frachet *et al.*, Hidden magnetism at the pseudogap critical point of a cuprate superconductor. *Nat. Phys.* **16**, 1064–1068 (2020).
10. S. Sachdev, J. Ye, Gapless spin-fluid ground state in a random quantum Heisenberg magnet. *Phys. Rev. Lett.* **70**, 3339–3342 (1993).
11. A. Y. Kitaev, "Talks at KITP, University of California, Santa Barbara" in *Entanglement in Strongly-Correlated Quantum Matter* (2015).
12. K. Haule, A. Rosch, J. Kroha, P. Wölfle, Pseudogaps in an incoherent metal. *Phys. Rev. Lett.* **89**, 236402 (2002).
13. K. Haule, A. Rosch, J. Kroha, P. Wölfle, Pseudogaps in the t - J model: An extended dynamical mean-field theory study. *Phys. Rev. B Condens. Matter Mater. Phys.* **68**, 155119 (2003).
14. D. Chowdhury, A. Georges, O. Parcollet, S. Sachdev, Sachdev-Ye-Kitaev models and beyond: A window into non-Fermi liquids. *arXiv [Preprint]* (2021).
15. D. G. Joshi, C. Li, G. Tarnopolsky, A. Georges, S. Sachdev, Deconfined critical point in a doped random quantum Heisenberg magnet. *Phys. Rev. X* **10**, 021033 (2020).
16. H. Guo, Y. Gu, S. Sachdev, Linear in temperature resistivity in the limit of zero temperature from the time reparameterization soft mode. *Ann. Phys.* **418**, 168202 (2020).
17. O. Parcollet, A. Georges, Non-Fermi-liquid regime of a doped Mott insulator. *Phys. Rev. B Condens. Matter Mater. Phys.* **59**, 5341–5360 (1999).
18. M. Tikhonovskaya, H. Guo, S. Sachdev, G. Tarnopolsky, Excitation spectra of quantum matter without quasiparticles II: Random t - J models. *Phys. Rev. B* **103**, 075142 (2021).
19. H. Shackleton, A. Wietek, A. Georges, S. Sachdev, Quantum phase transition at nonzero doping in a random t - J model. *Phys. Rev. Lett.* **126**, 136602 (2021).
20. P. T. Dumitrescu, N. Wentzell, A. Georges, O. Parcollet, Planckian metal at a doping-induced quantum critical point. *Phys. Rev. B* **105**, L180404 (2022).
21. A. Gourgout, *et al.*, Seebeck coefficient in a cuprate superconductor: Particle-hole asymmetry in the strange metal phase and Fermi surface transformation in the pseudogap phase. *Phys. Rev. X* **12**, 011037 (2022).
22. A. Georges, J. Mravlje, Skewed non-Fermi liquids and the Seebeck effect. *Phys. Rev. Res.* **3**, 043132 (2021).
23. M. Christos, F. M. Haehl, S. Sachdev, Spin liquid to spin glass crossover in the random quantum Heisenberg magnet. *Phys. Rev. B* **105**, 085120 (2022).
24. A. Georges, O. Parcollet, S. Sachdev, Quantum fluctuations of a nearly critical Heisenberg spin glass. *Phys. Rev. B Condens. Matter Mater. Phys.* **63**, 134406 (2001).